



# Axisymmetric finite element models for rotational molding

Axisymmetric  
finite element  
models

Lorraine G. Olson, George Gogos and  
Venkataramana Pasham

*Department of Mechanical Engineering, University of Nebraska,  
Lincoln, Nebraska, USA*

515

Received April 1998  
Revised January 1999  
Accepted February 1999

**Keywords** *Finite element, Heat transfer, Deposition, Profiles*

**Abstract** *We present a new nonlinear axisymmetric finite element model for heat transfer and powder deposition in rotational molding. Arbitrary Lagrangian Eulerian techniques are employed to track the gradual growth of the plastic layer. Results using this approach compare well with earlier 1-D models and with experimental data. Using the model to study the effects of locally enhanced heat transfer on part wall thickness, we find that controlling the relative magnitudes of radial and circumferential heat transfer is crucial in order to obtain desired wall thickness profiles.*

## Introduction

Rotational molding (also known as rotocasting or rotomolding) is a process used to manufacture hollow plastic products. Rotational molding is used to produce chemical tanks, automotive and commercial aircraft parts, backyard play equipment, toys, and many other items. It is an attractive alternative to injection and blow molding because the molds are inexpensive and the process can handle complex shapes, a wide range of part sizes, and variable thicknesses.

Figure 1 shows a schematic of the rotational molding process. In the first station (mold charging) very fine plastic powder (typically polyethylene) is placed in a metal mold, which is then closed. In the second station (heating), the mold is moved into an oven and rotated continuously about two axes. Speeds of rotation are relatively low, typically 10-20 rpm. As a result, the rotation distributes the powder to all areas of the mold by tumbling, rather than by centrifugal action. The heating of the plastic powder is accomplished by heating the mold from the outside. As the powder comes into contact with the hot mold it is first heated and then melts onto the mold, gradually covering all interior surfaces. The plastic layer continues to increase in thickness until all the powder has melted. The mold and plastic are further heated to consolidate the plastic. Oven set-point temperatures are typically 250-550°C, although the molds and parts typically only reach 200°C during the cycle. Eventually the still-rotating mold is moved from the heating station (oven) into the cooling station. The external surface of the mold is cooled by cold air jets, mist sprays, and water sprays. Finally, when the mold is cool, it is moved into the demolding station, the part is removed, and the cycle is complete. In practice, the stations are arranged in a ring, and charging and demolding occur in the same

physical location. An authoritative review on the subject of rotational molding of plastics can be found in Crawford (1996).

There are several theoretical heat transfer studies available in the literature on rotational molding. Rao and Throne (1972) presented an extensive analysis of various aspects of the rotational molding process. With respect to the thermal/fluid considerations, they proposed a complicated powder flow model to describe heat transfer to the powder. In a later paper, Throne (1976) proposed an alternative heat transfer model in which the powder was assumed to be in static contact with the mold surface at all times. The latter model showed better agreement with experimental data. More recently, Sun and Crawford (1993) developed a model to explore internal heating and cooling during rotational molding. In this model the plastic powder was treated as a static layer in contact with the mold and heat transfer from the mold to the powder was analyzed much like heat transfer in a packed particle bed. Nugent *et al.* (1992) compared this model to experimental results for a wide variety of processing conditions. In a recent series of papers, Gogos and Olson (Gogos *et al.*, 1997a; 1997b; 1998; 1999; Olson *et al.*, 1997) described a new theoretical model in which the powder is assumed to be well-mixed, and presented one-dimensional numerical approaches to the problem.

This paper reviews the theoretical model of Gogos and Olson and introduces a new finite element approach specially developed for the general axisymmetric numerical problem. This finite element method models both the heat transfer and the gradual powder deposition on the inner mold surface, and can be applied to a large number of realistic geometries. Because control of part wall thickness can be used to improve part designs for greater strength, the finite element techniques are then used to study the effects of spatially varying heat transfer on part thickness.

The governing differential equations for the mathematical model are reviewed in detail in the next section, and the numerical techniques employed to obtain solutions are described in the section "Finite element techniques". The following section, "Verification", describes the test cases employed to validate the model. A section on "Effects of locally enhanced heat transfer" applies the finite element techniques in examining the control of wall thickness to create internal ribs in parts. The final section gives conclusions and discusses future work.

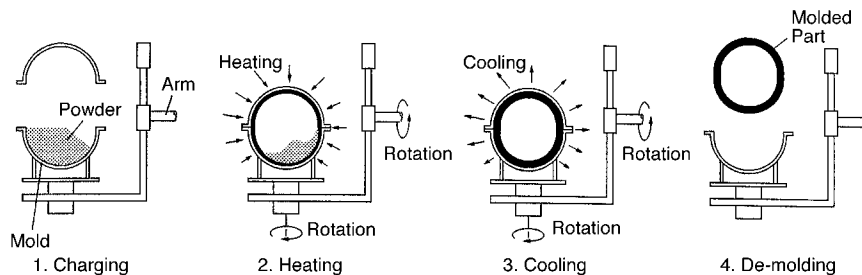


**Figure 1.**  
Rotational molding  
process stations

### Governing equations

For modeling purposes, rotational molding for parts of any geometry may be divided into three distinct phases (Gogos *et al.*, 1998). During phase 1 the mold is heated while spinning biaxially. Phase 1 is defined as lasting until the inside wall temperature of the mold locally reaches the melting temperature of the plastic. During phase 2 the available plastic powder is deposited as a molten layer on the inner surface. Phase 2 ends when all of the powder has been deposited. During phase 3 the molded plastic undergoes further heat transfer, solidifies, and eventually cools to the demolding temperature.

Although the equations can be written more generally, the following model assumes an axisymmetric geometry with constant material properties. Consequently, temperature is a function only of the radial coordinate, axial coordinate, and time. In addition, the current study addresses only phases 1 and 2 of the rotational molding process. (By the end of phase 2, the relative part wall thicknesses have been established. The viscosity of the molten plastic is so high that essentially no plastic migration occurs during phase 3.)

#### Phase 1

Figure 2 schematically indicates a typical geometry for phase 1, which is modeled as a straightforward transient heat conduction problem for the mold. The transient conduction equation in the mold region ( $V_m$ ) reduces to :

$$k_m \nabla^2 T = \rho_m c_m \frac{\partial T}{\partial t} \quad \text{in } V_m \quad (1)$$

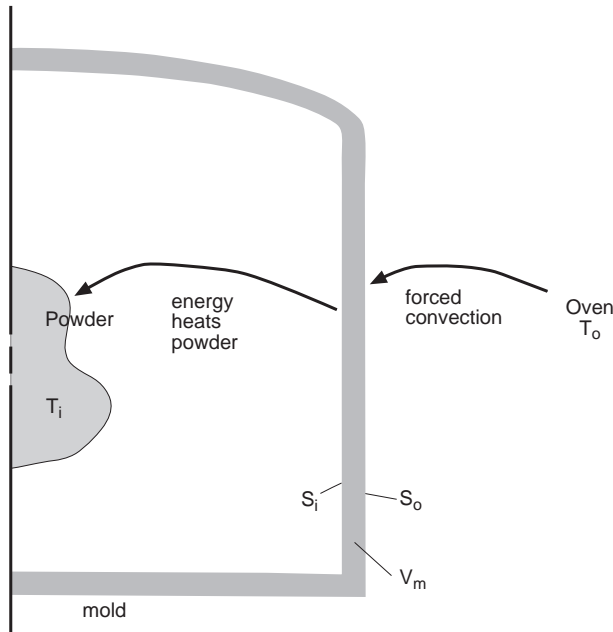


**Figure 2.**  
Geometry for phase 1

Here  $k_m$ ,  $\rho_m$ , and  $c_m$  are the conductivity, density, and specific heat of the mold respectively,  $T$  is the temperature of the mold, and  $t$  is time. Initially, the mold is assumed to be at some known ambient temperature,  $T_a$ .

The mold is placed in an oven which is assumed to be at a constant temperature  $T_o$ . Heat is transported due to convection at the outer ( $S_o$ ) and inner ( $S_i$ ) surfaces of the mold which is described by:

$$-k_m \frac{\partial T}{\partial n} = h_o [T - T_o] \quad \text{on } S_o \quad (2)$$

$$-k_m \frac{\partial T}{\partial n} = h_i [T - T_i] \quad \text{on } S_i \quad (3)$$

where  $T_i$  is the temperature of the well-mixed powder,  $h_i$  is the effective heat transfer coefficient for energy transfer to the powder from the mold,  $h_o$  is the external convection coefficient, and  $n$  is the unit outward normal from each surface. (The heat transfer parameters  $h_o$  and  $h_i$  may vary over each surface.)

The heat balance relation for the powder itself gives

$$m_p c_p \frac{dT_i}{dt} = \int_{S_i} h_i [T - T_i] dS_i \quad (4)$$

with  $m_p$  the mass of the powder and  $c_p$  the specific heat of the powder. Because of the assumption that the powder is well-mixed, and consequently has only a single effective temperature, this is the only equation for the powder and it involves the integral of the heat transported from the entire inner mold surface. In writing this equation, we have neglected the thermal capacitance of the air compared to the thermal capacitance of the powder. The initial temperature of the powder inside the mold is assumed to be the ambient temperature,  $T_i(0) = T_a$ . This phase ends when the inside surface of the mold locally reaches the melting temperature of the plastic,  $T_m$ .

### Phase 2

Figure 3 schematically indicates a typical geometry for this phase. Phase 2 begins when the powder that is in contact with the inner mold surface starts to melt and deposit on the inner surface. In our earlier work on spherical models for rotational molding (Gogos *et al.*, 1997a, 1997b, 1998, 1999; Olson *et al.*, 1997), phase 2 began at the same time for all points on the mold inner surface. However, in this study one of the crucial modifications is to allow the transition to phase 2 to occur at different times for different locations in the model.

In addition to the mold, the domain in phase 2 comprises a growing plastic layer on the inner mold surface. The heat transfer in the mold is governed by the same transient conduction equation, equation (1). The transient conduction equation for the plastic layer (region  $V_p$ ) which grows with time is described by



equation for the powder itself becomes

$$m_p c_p \frac{dT_i}{dt} = \int_{S_p} h_i [T_m - T_i] dS_p + \int_{S_i} h_i [T - T_i] dS_i \quad (8)$$

where

$$m_p = m_o - \int_{V_p} \rho_p dV_p \quad (9)$$

In equation (8), it is to be understood that the integral of the heat transferred to the powder is taken over the plastic inner surface ( $S_p$ ) plus any exposed inner mold surface ( $S_i$ ) where powder has not yet begun to deposit. This phase ends when all of the available powder ( $m_o$ ) deposits on the mold surface, i.e. when  $m_p = 0$ .

Note that the well-mixed assumption for the powder simplifies the model substantially. Rao and Throne (1972) investigated the effect of rotational speed on the powder-end time. They showed that this time decreases with increasing rotational speed and asymptotically approaches a constant value at about 10-20 rpm, which is within the range of typical rotational molding speeds. Hence, it can be inferred that the powder becomes well-mixed under typical conditions of rotational molding. In addition, it is clear from these 10-20 rpm rotational speeds that centrifugal effects and viscous dissipation within the thermoplastic powder are not likely to be significant in a heat transfer model for rotational molding.

### Finite element techniques

The governing equations presented above were solved using an arbitrary Lagrangian Eulerian finite element technique. Euler backward (fully implicit) time integration was employed, and at each time level a full Newton-Raphson iteration was employed to solve the nonlinear equations. In order to solve the equations by finite element techniques a "weak form" of the governing equations is created, the domain is discretized into finite elements and element matrices are calculated, and finally the element contributions are assembled and solved. These steps are given in more detail in what follows.

#### *Weak forms*

In phase 1 the problem is a linear transient conduction problem. The weak form for the conduction in the mold, including the exterior and interior convection boundary conditions, becomes

$$\int_{V_m} k_m \nabla \bar{T} \cdot \nabla T dV_m + \int_{V_m} \rho_m c_m \bar{T} \frac{\partial T}{\partial t} dV_m$$

$$+ \int_{S_o} \bar{T} h_o [T - T_o] dS_o - \int_{S_i} \bar{T} h_i [T - T_i] dS_i = 0 \quad (10)$$

Here a bar over a variable indicates a virtual variation in that variable, in the usual finite element sense (Bathe, 1996). For the powder itself the weak form is simply

$$\bar{T}_i m_p c_p \frac{dT_i}{dt} - \int_{S_i} \bar{T}_i h_i [T - T_i] dS_i = 0 \quad (11)$$

Plastic deposition begins during phase 2, and the motion of the plastic free surface is taken into account by an arbitrary Lagrangian Eulerian (ALE) technique (see, for example, Nikitpaiboon and Bathe, 1993; Ghosh and Moorthy, 1993; Hu and Liu, 1993; Liu *et al.*, 1992; Nomura and Hughes, 1993; Ghosh and Kikuchi, 1991). In an ALE approach nodal point movement is independent of the movement of the material itself, and may be specified to reduce mesh distortion. For our models this reduces to “stretching” the existing mesh in a time-dependent fashion during the analysis to cover the entire plastic region, and modifying the calculation of the time derivatives so that

$$\frac{\partial T}{\partial t} = \frac{dT_{node}}{dt} - \dot{\mathbf{x}}_{node} \cdot \nabla T \quad (12)$$

where  $\frac{dT_{node}}{dt}$  is the rate of change of the temperature with time following the nodal point, and  $\dot{\mathbf{x}}_{node}$  is the velocity vector for the node.

The weak form for the mold and plastic becomes

$$\begin{aligned} & \int_{S_o} \bar{T} h_o [T - T_o] dS_o + \int_{V_m} k_m \nabla \bar{T} \cdot \nabla T dV_m + \int_{V_m} \rho_m c_m \bar{T} \frac{\partial T}{\partial t} dV_m \\ & + \int_{V_p} k_p \nabla \bar{T} \cdot \nabla T dV_p + \int_{V_m} \rho_p c_p \bar{T} \frac{\partial T}{\partial t} dV_p \\ & + \int_{S_i} \bar{T} h_i [T - T_i] dS_i + \int_{S_p} \bar{T} h_i [T - T_i] dS_p + \int_{S_p} \bar{T} \rho_p (\dot{\mathbf{x}}_S \cdot \mathbf{n}) \\ & [c_p (T_m - T_i) + L] dS_p = 0 \end{aligned} \quad (13)$$

where it is understood that equation (12) is used in the transient integral for the plastic. In equation (13) the integral over  $S_i$  is implied to be only over the exposed surface of the mold, where powder deposition has not yet begun. Notice that this weak form includes the exterior boundary condition (equation (2)), the mold/molten plastic heat balance, the molten plastic/powder heat flux balance (equation (7)), and the heat transfer from the exposed mold surface

(equation (3)). The plastic surface temperature condition (equation (6)) is used to determine the new position of the plastic free surface during the nonlinear iteration.

The weak form for the powder itself is written as

$$\bar{T}_i m_p c_p \frac{dT_i}{dt} - \int_{S_p} \bar{T}_i h_i [T_m - T_i] dS_p - \int_{S_i} \bar{T}_i h_i [T - T_i] dS_i \quad (14)$$

and the mass of the powder is adjusted in each iteration according to equation (9). Once again, the integral over  $S_i$  is implied to be only over the exposed surface of the mold, where powder deposition has not yet begun.

*Finite element discretization and matrices*

*Phase 1 discretization.* Figure 4 shows a typical finite element discretization of the axisymmetric domain for phase 1. The discretized domain comprises exterior elements, mold elements, plastic elements and the interior elements. The exterior convection boundary condition is handled by linear (two-node or three-node) elements with two unknown temperatures (since  $T_o$  is known). The three-node or four-node interior element accounts for the powder equation (equation (11)), as well as the internal convection on the mold. As many mold elements (three-node, four-node, six-node, eight-node or nine-node) as required

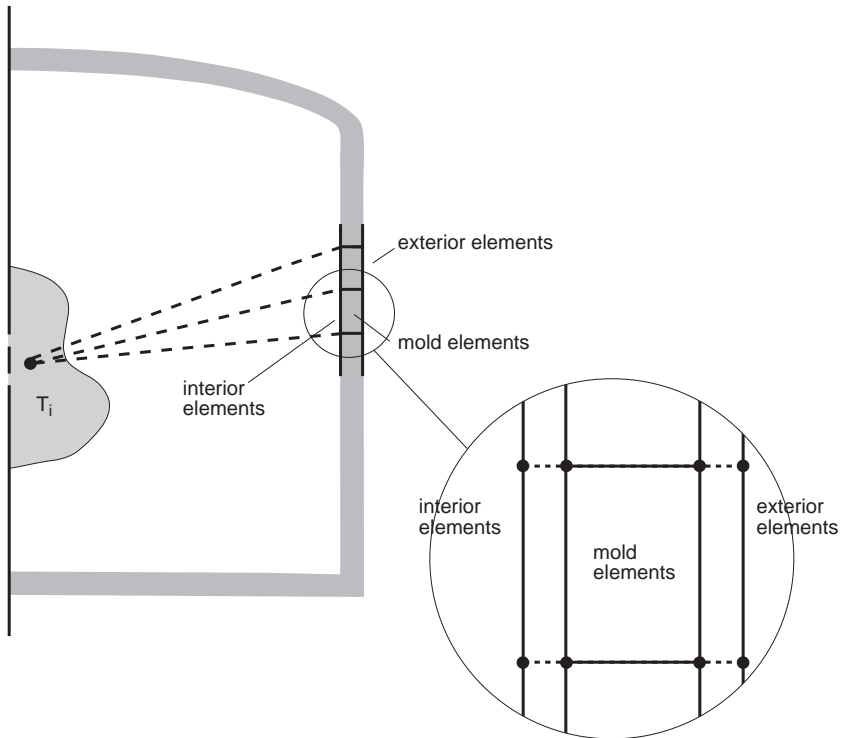


**Figure 4.**  
Finite element  
discretization for  
phase 1

can be used to capture the temperature variation in the solid mold. In typical rotational molding analyses the temperature is nearly uniform across the thickness of the mold and very few elements are required for accuracy. In phase 1, the plastic elements are collapsed onto the inner surface of the mold – they have zero size and uniform temperature[1]. Although these elements are not used in phase 1, their presence allows a seamless transition to phase 2, when they will begin to grow.

Using standard finite element techniques (Bathe, 1996), the element matrices can be derived. The element matrices consist of the element forcing vector, element stiffness matrix, and the element mass matrix.

*Phase 1: mold elements.* We discretize the mold terms in the weak form using standard isoparametric shape functions. In our implementation they may have three or six nodes if they are triangular, and may have four, eight or nine nodes if they are quadrilaterals. In any case, the temperature, radial coordinate, and axial coordinates are given by

$$T = \mathbf{NT}, \quad r = \mathbf{Nr}, \quad \text{and} \quad z = \mathbf{Nz} \quad (15)$$

where

$$\mathbf{N} = [N_1 \ N_2 \ \dots \ N_l], \quad \mathbf{T}^T = [T_1 \ T_2 \ \dots \ T_l],$$

$$\mathbf{r}^T = [r_1 \ r_2 \ \dots \ r_l], \quad \mathbf{z}^T = [z_1 \ z_2 \ \dots \ z_l],$$

- $N_j$  = shape function for node j,
- $T_j$  = temperature of node j,
- $r_j$  = radial coordinate of node j,
- $z_j$  = axial coordinate of node j,
- $l$  = number of nodes per finite element.

The forcing vector for the mold elements can be written from the weak form as,

$$\mathbf{F}_{mold}^e = \int_{-1}^1 \int_{-1}^1 k_m \mathbf{B}^T \left[ c \frac{\partial T}{\partial r} \frac{\partial T}{\partial z} \right] r |\mathbf{J}| dq ds + \int_{-1}^1 \int_{-1}^1 \rho_m c_m \mathbf{N}^T \frac{\partial T}{\partial t} r |\mathbf{J}| dq ds \quad (16)$$

where

$$\mathbf{B} = \mathbf{J}^{-1} \begin{bmatrix} \frac{\partial N_1}{\partial q} & \dots & \frac{\partial N_l}{\partial q} \\ \frac{\partial N_1}{\partial s} & \dots & \frac{\partial N_l}{\partial s} \end{bmatrix}$$

and the Jacobian is given by

$$\mathbf{J} = \begin{bmatrix} \frac{\partial r}{\partial q} & \frac{\partial z}{\partial q} \\ \frac{\partial r}{\partial s} & \frac{\partial z}{\partial s} \end{bmatrix}.$$

(Here we use  $q$  and  $s$  as the local coordinate system within a finite element.)  
The element stiffness matrix for the mold elements is given by

$$\mathbf{K}_{mold}^e = \int_{-1}^1 \int_{-1}^1 k_m \mathbf{B}^T \mathbf{B} r |\mathbf{J}| dq ds, \quad (17)$$

while the element mass matrix for the mold elements is

$$\mathbf{M}_{mold}^e = \int_{-1}^1 \int_{-1}^1 \rho_m c_m \mathbf{N}^T \mathbf{N} r |\mathbf{J}| dq ds. \quad (18)$$

*Phase 1: exterior elements.* The exterior elements are typical convection elements, either 2-node or 3-node line elements. The forcing vector for the exterior elements reduces to,

$$\mathbf{F}_{ext}^e = \int_{-1}^1 h_o \mathbf{N}^T (T - T_o) r |\mathbf{J}| ds \quad (19)$$

where  $s$  is the local coordinate within the line element and  $\mathbf{J}$  is the usual one-dimensional element Jacobian matrix. The stiffness matrix for the one dimensional exterior elements is

$$\mathbf{K}_{ext}^e = \int_{-1}^1 h_o \mathbf{N}^T \mathbf{N} r |\mathbf{J}| ds \quad (20)$$

*Phase 1: interior elements.* All the interior elements contain two or three surface nodes and share a common powder node which lies at an arbitrary location, often taken near the geometrical center. The forcing vector for the interior element has two components:

$$\mathbf{F}_{int}^e = \begin{bmatrix} \mathbf{F}_s \\ \mathbf{F}_i \end{bmatrix} \quad (21)$$

The  $\mathbf{F}_s$  term acts on the (two or three) surface nodal temperatures, while  $\mathbf{F}_i$  acts on the powder node temperature. These components can be given by

$$\mathbf{F}_s = \int_{-1}^1 h_i \mathbf{N}^T (T - T_i) r |\mathbf{J}| ds \quad (22)$$

and

$$\mathbf{F}_i = \frac{m_p c_p}{2\pi E_{int}} \frac{dT_i}{dt} - \int_{-1}^1 h_i (T - T_i) r |\mathbf{J}| ds \quad (23)$$

Here  $E_{int}$  is the total number of interior elements, and appears in equation (23) to correct the total assembled powder mass. Note that the integral in the powder term (equation (23)) is still over the surface element.

The stiffness matrix for the interior elements is then given by

$$\mathbf{K}_{int}^e = \begin{bmatrix} \mathbf{K}_{ss} & \mathbf{K}_{si} \\ \mathbf{K}_{si}^T & \mathbf{K}_{ii} \end{bmatrix} \quad (24)$$

where  $\mathbf{K}_{ss}$  acts on the (two or three) surface nodes,  $\mathbf{K}_{ii}$  acts on the powder node, and  $\mathbf{K}_{si}$  couples the two sets of nodes. The corresponding stiffness entries are given by

$$\mathbf{K}_{ss} = \int_{-1}^1 h_i \mathbf{N}^T \mathbf{N} r |\mathbf{J}| ds \quad (25)$$

$$\mathbf{K}_{ii} = \int_{-1}^1 h_i r |\mathbf{J}| ds \quad (26)$$

and

$$\mathbf{K}_{si} = - \int_{-1}^1 h_i \mathbf{N}^T r |\mathbf{J}| ds \quad (27)$$

The mass matrix has a similar structure, but only the term corresponding to the powder temperature is non-zero:

$$\mathbf{M}_{ii} = \frac{m_p c_p}{2\pi E_{int}} \quad (28)$$

*Phase 2 discretization.* Figure 5 shows a typical finite element discretization of the axisymmetric domain for phase 2. No new elements are introduced in phase 2, but two changes are made in the calculations performed. The interior elements now begin to move inward at a rate determined by the melting of the powder, and the plastic elements expand inwards in proportion to the motion of the interior elements.

In addition, the mass of the powder decreases with time and hence a degree-of-freedom associated with the mass is introduced. The element matrices for the mold and exterior elements are unchanged.

*Phase 2: interior elements.* Once phase 2 begins, the interior elements move inward to account for the accumulating plastic layer. Consequently, each surface node has radial and axial displacement unknowns as well as a temperature degree-of-freedom.

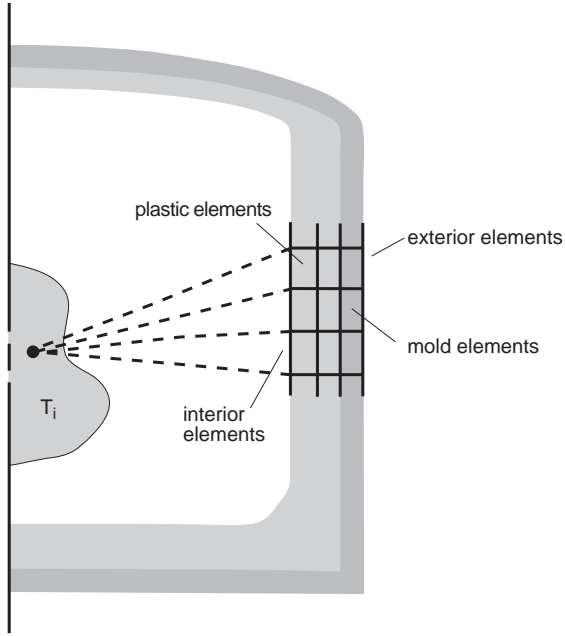


**Figure 5.**  
Finite element  
discretization for  
phase 2

The forcing vector for the interior element now contains four terms:

$$\mathbf{F}_{int}^e = \begin{bmatrix} \mathbf{F}_s \\ \mathbf{F}_i \\ \mathbf{F}_r \\ \mathbf{F}_z \end{bmatrix} \quad (29)$$

where

$$\mathbf{F}_s = \int_{-1}^1 h_i \mathbf{N}^T (T - T_i) r |\mathbf{J}| ds + \int_{-1}^1 \mathbf{N}^T \rho_p (\dot{\mathbf{x}}_S \cdot \mathbf{n}) (c_p (T_m - T_i) + L) r |\mathbf{J}| ds \quad (30)$$

and

$$\mathbf{F}_i = \frac{m_p c_p}{2\pi E_{int}} \frac{\partial T}{\partial t} - \int_{-1}^1 h_i (T - T_i) r |\mathbf{J}| ds \quad (31)$$

These terms couple the energy from the surface and the energy to the powder. The movement of the nodes is governed by the second two forcing terms:

$$\mathbf{F}_r = \begin{bmatrix} (T_m - T_1)n_{r_1} \\ (T_m - T_2)n_{r_2} \\ \dots\dots\dots \\ (T_m - T_l)n_{r_l} \end{bmatrix} \quad (32)$$

$$\mathbf{F}_z = \begin{bmatrix} (T_m - T_1)n_{z_1} \\ (T_m - T_2)n_{z_2} \\ \dots\dots\dots \\ (T_m - T_l)n_{z_l} \end{bmatrix} \quad (33)$$

Here,  $T_l$  is the temperature at a surface node, and  $n_{r_l}$  and  $n_{z_l}$  are the radial and axial components of the element normals evaluated at the surface nodes. This ensures that the nodes move normal to the surface, and that the motion for a node stops when the temperature of that node reaches  $T_m$ . In addition, the motion at a node associated with two adjacent surface elements will contain the sum of the two local normals once the elements are assembled.

The stiffness matrix is written as

$$\mathbf{K}_{int}^e = \begin{bmatrix} \mathbf{K}_{ss} & \mathbf{K}_{si} & 0 & 0 \\ \mathbf{K}_{si}^T & \mathbf{K}_{ii} & 0 & 0 \\ 0 & 0 & \mathbf{K}_{rr} & 0 \\ 0 & 0 & 0 & \mathbf{K}_{zz} \end{bmatrix} \quad (34)$$

The  $\mathbf{K}_{ss}$ ,  $\mathbf{K}_{si}$ , and  $\mathbf{K}_{ii}$  terms are identical to those in phase 1 (equations (25), (27) and (26)).

The  $\mathbf{K}_{rr}$  and  $\mathbf{K}_{zz}$  terms, in our current formulation, are simply penalty terms given as

$$\mathbf{K}_{rr} = K_{BIG} \begin{bmatrix} 1 & 0 & \dots & 0 \\ 0 & 1 & \dots & 0 \\ \dots & \dots & \dots & 0 \\ 0 & 0 & 0 & 1 \end{bmatrix} \quad (35)$$

$$\mathbf{K}_{zz} = K_{BIG} \begin{bmatrix} 1 & 0 & \dots & 0 \\ 0 & 1 & \dots & 0 \\ \dots & \dots & \dots & 0 \\ 0 & 0 & 0 & 1 \end{bmatrix} \quad (36)$$

Note that the normal displacement of a surface node in any given iteration is therefore given by the temperature error  $(T - T_m)$  divided by  $K_{BIG}$ . By adjusting  $K_{BIG}$ , the user can select how rapidly the surface nodes iterate towards the equilibrium configuration within any given time step. Small values imply large steps, but can cause severe overshoots and consequent instabilities.

Large values of  $K_{BIG}$  imply small steps and good stability, but can result in significant increases in computational time. (A typical value of  $K_{BIG}$  for the cases examined in this paper was  $8.1 \times 10^6$ .)

The mass matrix has only a single non-zero term, which associated with the powder mass

$$\mathbf{M}_{ii} = \frac{m_p c_p}{2\pi E_{int}}, \quad (37)$$

where  $m_p$  is the current mass of the powder.

*Phase 2: plastic elements.* Plastic elements are discretized using the standard isoparametric shape functions. In our implementation they may have three or six nodes if they are triangular, and may have four, eight or nine nodes if they are quadrilaterals. Plastic elements have three degrees-of-freedom per node, in general – two displacements and one temperature. In our current implementation the displacement of the plastic nodes is handled completely by constraint equations, and no terms appear in the element matrices corresponding to those unknowns. Hence the element matrices for the plastic are quite similar to those of the mold:

$$\mathbf{F}_{plas}^e = \int_{-1}^1 \int_{-1}^1 k_p \mathbf{B}^T \left[ c \frac{\partial T}{\partial r} \frac{\partial T}{\partial z} \right] r |\mathbf{J}| dq ds + \int_{-1}^1 \int_{-1}^1 \rho_p c_p \mathbf{N}^T \frac{\partial T}{\partial t} r |\mathbf{J}| dq ds \quad (38)$$

$$\mathbf{K}_{plas}^e = \int_{-1}^1 \int_{-1}^1 k_p \mathbf{B}^T \mathbf{B} r |\mathbf{J}| dq ds \quad (39)$$

$$\mathbf{M}_{plas}^e = \int_{-1}^1 \int_{-1}^1 \rho_p c_p \mathbf{N}^T \mathbf{N} r |\mathbf{J}| dq ds \quad (40)$$

Note that the  $\frac{\partial T}{\partial t}$  term in the forcing vector (equation (38)) is handled as in equation (12).

In addition, it is necessary to track the total mass of the deposited plastic. This is calculated by integrating the mass of the individual plastic elements, and summing the contributions in the forcing vector for the plastic elements

$$\mathbf{F}_m = \int_{-1}^1 \int_{-1}^1 \rho_p r |\mathbf{J}| dq ds \quad (41)$$

This entry is simply used to accumulate the total mass consumed thus far in the analysis, and hence we use  $\mathbf{K}_{mm} = 1$  to insert it into the structure of the differential equations.

*Solution of assembled matrices*

Once the element terms are calculated, they are assembled into global stiffness, mass, and forcing vectors. Although the equations for phase 1 are linear, they are solved by iteration to allow a seamless transition to phase 2. Hence, at each time step we iterate (using a Newton-Rhapson iteration) on the implicit time equation (Bathe, 1996):

$${}^t\mathbf{X}^0 = {}^{t-\Delta t}\mathbf{X} + {}^{t-\Delta t}\dot{\mathbf{X}}\Delta t \quad (42)$$

$$\left(\mathbf{K} + \frac{1}{\Delta t}\mathbf{M}\right)^i \Delta\mathbf{X}^i = -{}^t\mathbf{F}^i \quad (43)$$

$${}^t\mathbf{X}^i = {}^t\mathbf{X}^{i-1} + \Delta\mathbf{X}^i \quad (44)$$

where  $\Delta t$  is the time step size, the right superscript  $i$  is for the iteration number within a single time step, and the left superscript  $t$  indicates the time level. Once the change in the  $\mathbf{X}$  vector is small (when  $\mathbf{F}$  is nearly zero) the iteration at this time level is terminated and the time level is incremented.

**Verification**

*Spherical mold*

In our previous studies of rotational molding (Gogos *et al.*, 1997a, 1997b, 1998, 1999; Olson *et al.*, 1997), we developed a “base case” for our spherically symmetric finite difference model, in which polyethylene powder is rotationally molded within a spherical steel mold. The inner radius of the mold was 0.214m and the mold thickness was 0.0021m. The parameter values for the base case are shown in Table I. These property values were estimated from data available in the literature (Nugent 1990; Tadmor and Gogos 1979; Nugent *et al.*, 1992) and are thus somewhat approximate.

For the current study, we initially tested a full axisymmetric finite element model of this base case against the 1-D spherically symmetric finite difference model. The results obtained were excellent, with axisymmetric finite element results for mold and powder temperatures within 1 per cent of the spherically symmetric finite difference results at all times.

*Cylindrical base case mold*

In Nugent’s experiments (1990), a “cube” mold with a large flange was employed in the tests. We created the spherical base case model for our previous papers (Gogos *et al.*, 1997a, 1997b, 1998, 1999; Olson *et al.*, 1997) by matching the mass and surface area of the cube mold. In a similar fashion, the axisymmetric model shown in Figure 6 was developed: each portion (top, sides, base, flange) of the mold was matched for surface area and volume with its counterpart in the cube mold.

HF  
9,5

Mold parameters

$c_m = 490\text{J}/(\text{kg}\cdot\text{K})$   
 $k_m = 56.3\text{W}/(\text{m}\cdot\text{K})$   
 $\rho_m = 7,830\text{kg}/\text{m}^3$

530

Plastic parameters

$c_p = 2,430\text{J}/(\text{kg}\cdot\text{K})$   
 $k_p = 0.23\text{W}/(\text{m}\cdot\text{K})$   
 $\rho_p = 751\text{kg}/\text{m}^3$   
 $L = 180,000\text{J}/\text{kg}$   
 $m_o = 1.49\text{kg}$   
 $T_m = 128^\circ\text{C}$

Heat transfer coefficients

$h_i = 5.0\text{W}/(\text{m}^2 \cdot \text{K})$   
 $h_o = 19.3\text{W}/(\text{m}^2 \cdot \text{K})$  for air

**Table I.**  
Parameters for base  
case testing

Other parameters

$T_a = 25.2^\circ\text{C}$   
 $T_o = 330^\circ\text{C}$

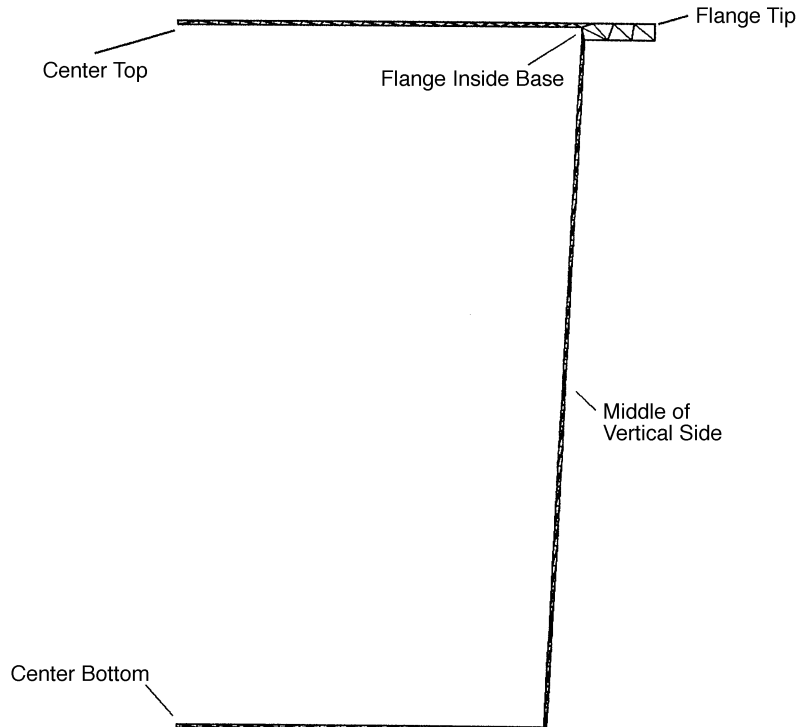


**Figure 6.**  
Mesh geometry for  
axisymmetric base case  
analysis

This axisymmetric model was employed, with the other base case parameters, to obtain temperature and plastic layer thickness results as a function of time. The difference in temperature between the center top, the center bottom, and the middle of the vertical sides is very slight, reaching a maximum of only 1°C by the end of phase 2. (Figure 6 indicates the locations under discussion.) The temperature difference between the flange tip and the flange inside base is somewhat larger, reaching a maximum of 5°C at the end of phase 2. However, Figure 7 shows the substantial differences in temperature between the center top and the flange inside base. The center top temperature rises at a substantially higher rate than the flange inside base in phase 1, but rises much more slowly in phase 2 so that by the end of phase 2 the center top is actually 14°C cooler than the flange inside base. Figure 7 also shows the spherical model results for the base case, which lie between the two axisymmetric model extremes for the first 250 seconds, but which actually fall below the axisymmetric model toward the end of phase 2. The temperatures predicted by the axisymmetric model agree well with experimental data (scanned electronically from Nugent (1990)). Figure 8 shows the plastic thickness shortly after the onset of phase 2, at time 250 seconds. (Plastic layer shown ten times mold scale.) The cooler flange area has not yet seen substantial plastic deposition, although the walls far from the corners have a coating of molten plastic. However, by the end of the molding cycle, the plastic layer is mostly uniform along the inner surface of the mold.

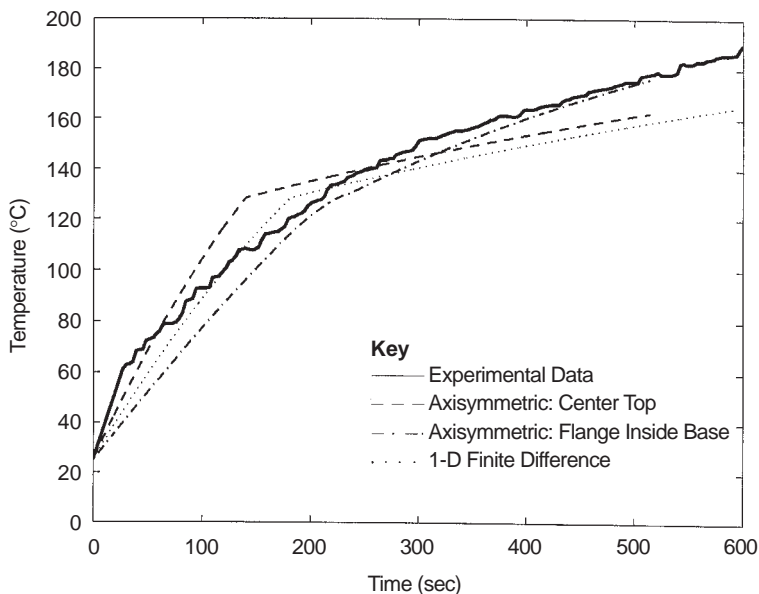


**Figure 7.**  
Temperature results for  
base case analysis

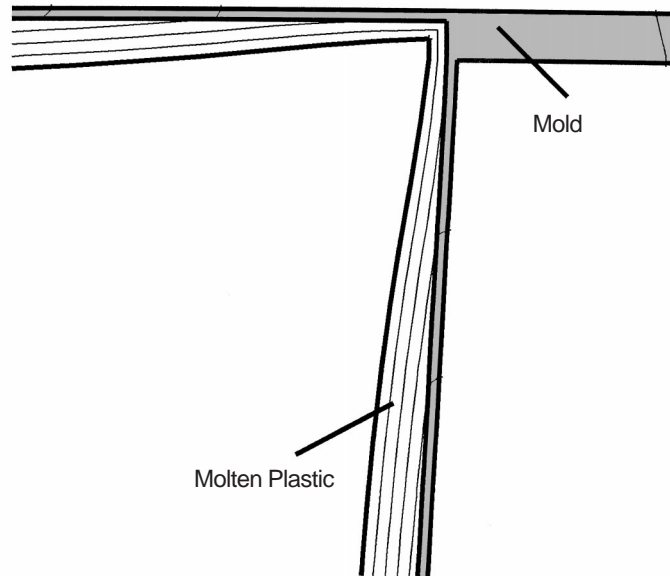


**Figure 8.** Non-uniform deposition of molten plastic near flange, with temperature contours. Axisymmetric finite element model for base case analysis, time 250 seconds. Contour lines at 130, 132, 134, 136° C. Plastic layer shown ten times mold scale

### Effects of locally enhanced heat transfer

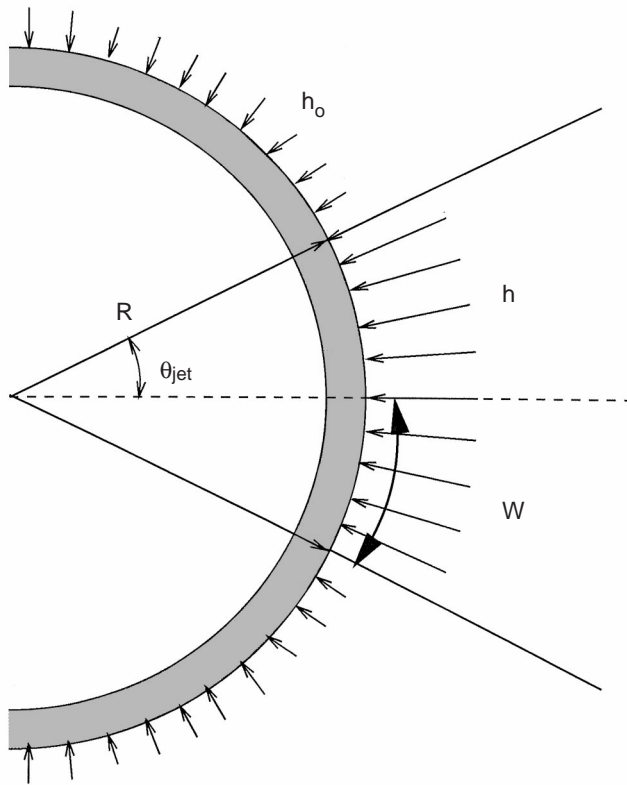
In practice, air jets (“air amplifiers” or “transvectors”) are employed to enhance the heat transfer at selected locations on the mold surface, allowing thin part walls to be thickened locally. This can be used to improve part quality near difficult mold contours, or to increase part thickness in high stress regions. In this section we will examine the effect of locally enhanced heat transfer on the ability to create “internal ribs” in an otherwise uniform spherical part. Our focus will be on which heat transfer parameters control the size and shape of the ribs.

Figure 9 indicates the geometry under consideration. We consider a spherical mold with an external heat transfer coefficient  $h_o$  over the majority of its surface. In a region of width  $w$  near the centerline of the sphere, the heat transfer coefficient is increased to  $h$ . The spherical base case is used as the starting point for the analysis, so that  $R = 0.214\text{m}$ , the mold thickness is  $\delta_m = 0.0021\text{m}$ , and the other parameters are given in Table I.

For our original spherical base case model studies, there were eight dimensionless groups of interest which are reviewed in Table II (Gogos *et al.*, 1998). Here we have introduced only two new variables to the original base case problem, which may be accounted for in two new dimensionless groups:

- the angle  $w/R = \theta_{jet}$ ; and
- the relative heat transfer coefficient  $hw/h_oR$ .

Figure 10 shows the final plastic layer profile for the base case, when  $w/R$  is held fixed at 0.077 (approximately  $4^\circ$ ) and the relative heat transfer coefficient is varied. Notice that the size of the ribs is quite large, with the plastic thickness



**Figure 9.**  
Geometry for study of  
locally enhanced heat  
transfer

$\Pi_2 = \frac{T_m - T_a}{T_o - T_a}$	Plastic melting temperature
$\Pi_3 = \frac{\rho_p c_p \delta_p}{\rho_m c_m \delta_m}$	Plastic to mold thermal capacitance ratio
$\Pi_4 = \frac{h_i}{h_o}$	Inside to outside heat transfer coefficient ratio
$\Pi_5 = \frac{L}{c_p (T_o - T_a)}$	Energy required for phase change
$\Pi_6 = \frac{k_p}{\delta_p h_o}$	Plastic conductance
$\Pi_7 = \frac{\delta_m}{R}$	Mold curvature effect
$\Pi_8 = \frac{k_m}{\delta_m h_o}$	Mold conductance
$\Pi_9 = \frac{\delta_p}{R}$	Plastic curvature effect

**Table II.**  
Dimensionless groups  
associated with heat  
transfer to spherical  
base case

( $\delta$ ) equaling its mean value ( $\delta_p$ ) at an angle of roughly  $20^\circ$ . This is true regardless of the relative heat transfer coefficient, and despite the fact that the enhanced region itself is only  $4^\circ$ . In fact, varying the enhanced region size has little effect on the ribs, as shown in Figure 11. Here the width of the enhanced heat transfer region varies from approximately  $1^\circ$  up to  $9^\circ$ , with little effect on

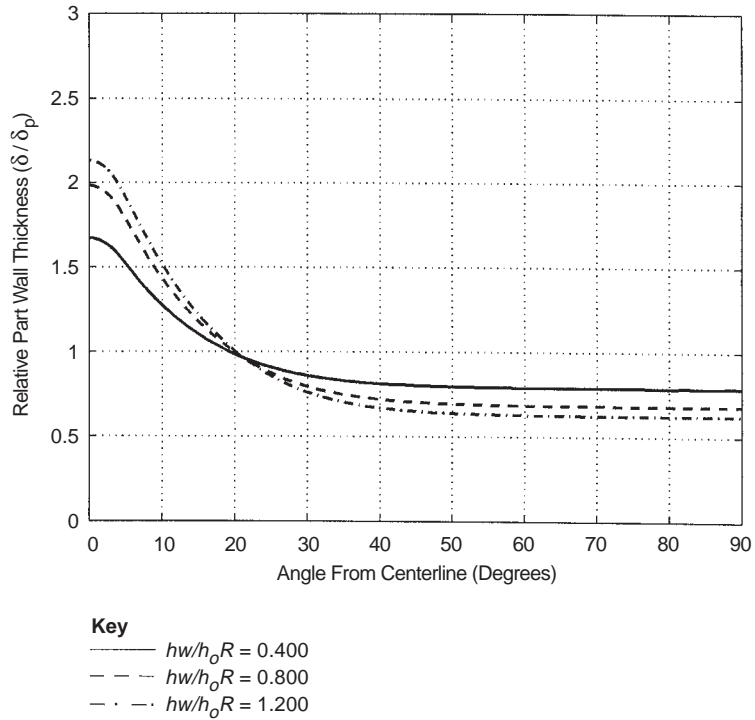


**Figure 10.** Effect of relative heat transfer coefficient on final plastic layer profiles. Base case with  $w/R = 0.077$  ( $4^\circ$ )

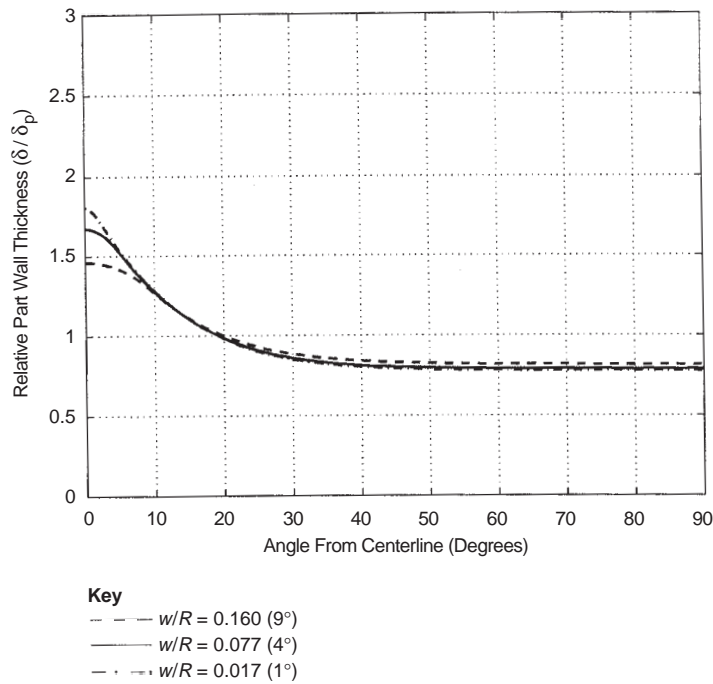


**Figure 11.** Effect of jet width  $w/R$  on final plastic layer profiles. Base case with  $hw/h_oR = 0.400$

the rib shape itself. This appears to be due to the rate of thermal diffusion in the metal wall of the mold, which controls the size of the heated zone far more strongly than the patterns we attempted to impose.

Next, we examined the effects on the plastic layer profiles of variations in the original eight dimensionless groups. Figures 12 through 19 give the plastic layer profiles. Several dimensionless parameters have essentially no effect: plastic melting temperature ( $\Pi_2$ , Figure 12), inside to outside heat transfer coefficient ratio ( $\Pi_4$ , Figure 14), energy required for phase change ( $\Pi_5$ , Figure 15), and plastic curvature effect ( $\Pi_9$ , Figure 19).

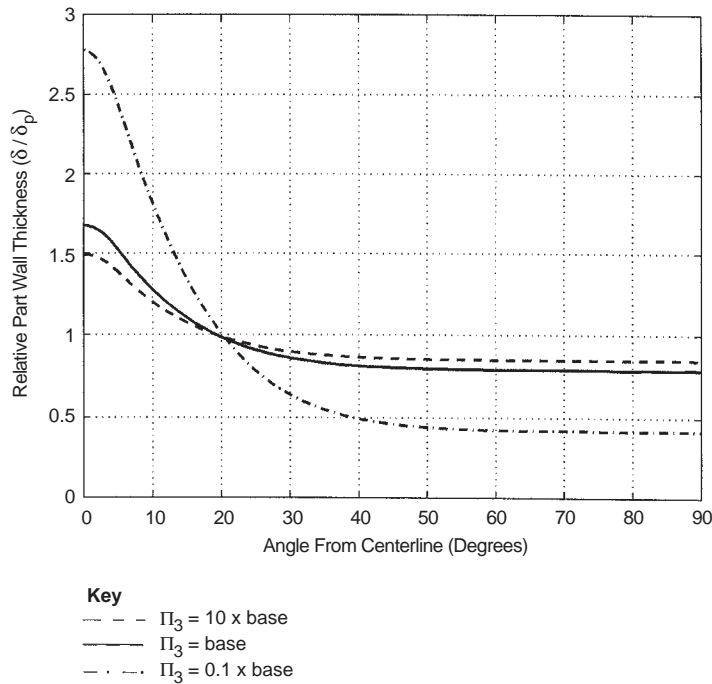
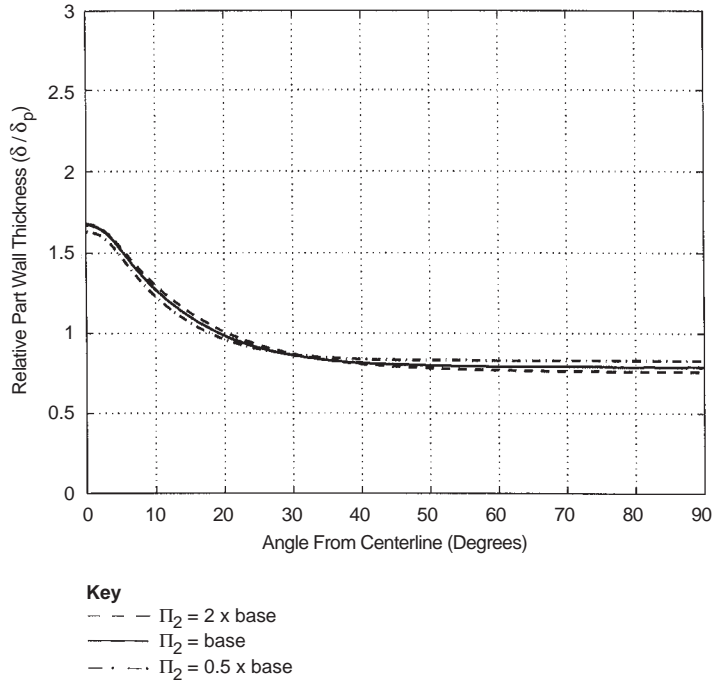
As shown in Figure 13, the plastic to mold thermal capacitance ratio ( $\Pi_3$ ) has a strong effect on the amplitude of the rib, but almost no effect on the width – the plastic layer thickness equals its nominal thickness at approximately  $20^\circ$  over a range of 100 times change in  $\Pi_3$ . The capacitance of the plastic layer appears to have a large effect on how much plastic deposits in a given region, but not on the extent of the region itself.

The plastic conductance ( $\Pi_6$ , Figure 16) and the mold conductance ( $\Pi_8$ , Figure 18) show opposite trends. A high plastic conductance produces a somewhat narrower and sharper rib, as does a low mold conductance. Conversely, low plastic conductance and high mold conductance produce a very wide, smoothed-out “rib”.

The most unexpected result was the extremely strong effect of  $\delta_m/R$  ( $\Pi_7$ , Figure 17), which we have called the mold curvature effect. In our previous studies (Gogos *et al.*, 1997a, 1997b, 1998, 1999; Olson *et al.*, 1997) we found that the mold curvature had essentially no effect on the time required for powder deposition in a spherically symmetric system. Here we see a strong effect, which we explain as diagrammed in Figure 20. Heat from the oven enters the mold, and follows two paths in this multidimensional case: circumferential heat flow and radial heat flow. The relative resistances of these two paths determines the amount of heat flow in each direction, and controls the circumferential temperature gradients which themselves determine the plastic deposition region. High plastic conductance or low mold conductance favor radial heat flow, and the high temperature regions on the wall are small (narrow, sharp ribs). Low plastic conductance or high mold conductance favor circumferential heat flow, which reduces the circumferential heat gradients and produces wide, smeared ribs.

$\delta_m/R$  is significant in this context because it is varied while other parameters are held fixed. Molds which are thin compared to their radius will tend to reproduce the enhanced heat transfer region as a sharp internal rib, because circumferential heat transfer is suppressed. Molds which are thick compared to their radius allow substantial circumferential heat transfer and produce ribs which are not sharply defined.

These observations allow us to take the original base case mold and modify it to produce well-defined ribs. The original mild steel mold material is replaced by a low conductivity AISI 347 stainless steel ( $\rho_m = 7,980\text{kg/m}^3$ ,  $c_m = 480\text{J/kg K}$ ,  $k_m = 14.2\text{W/mK}$ ) (Schmidt *et al.*, 1993). In addition, the mold thickness is



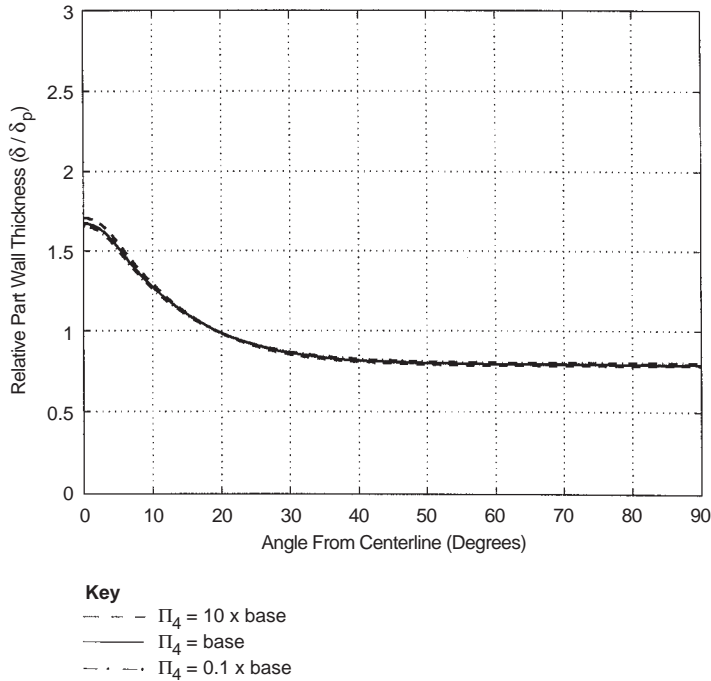


**Figure 14.**  
Effect of variations in  $\Pi_4 = h_i h_o$  on plastic layer profiles. Base case with  $hw/h_o R = 0.400$  and  $w/R = 0.077$  ( $4^\circ$ )

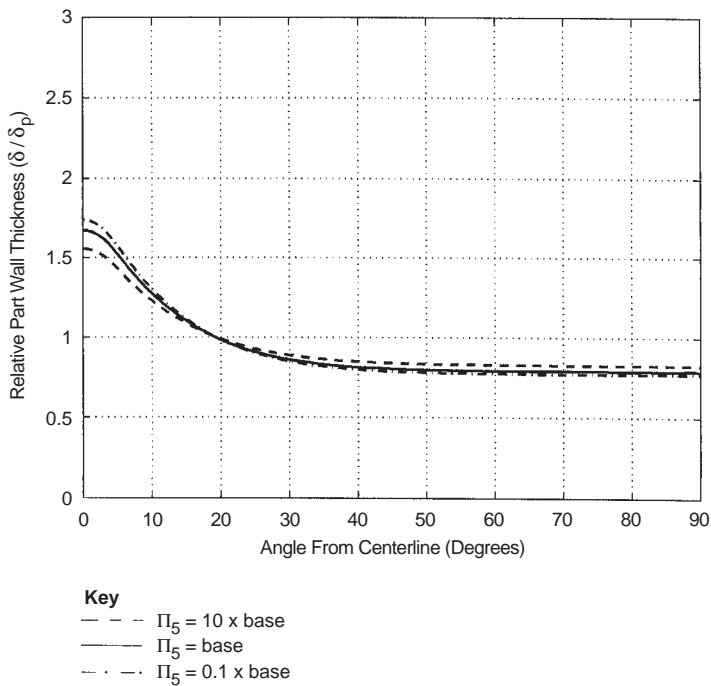


**Figure 15.**  
Effect of variations in  $\Pi_5 = L/(c_b(T_o - T_a))$  on plastic layer profiles. Base case with  $hw/h_o R = 0.400$  and  $w/R = 0.077$  ( $4^\circ$ )

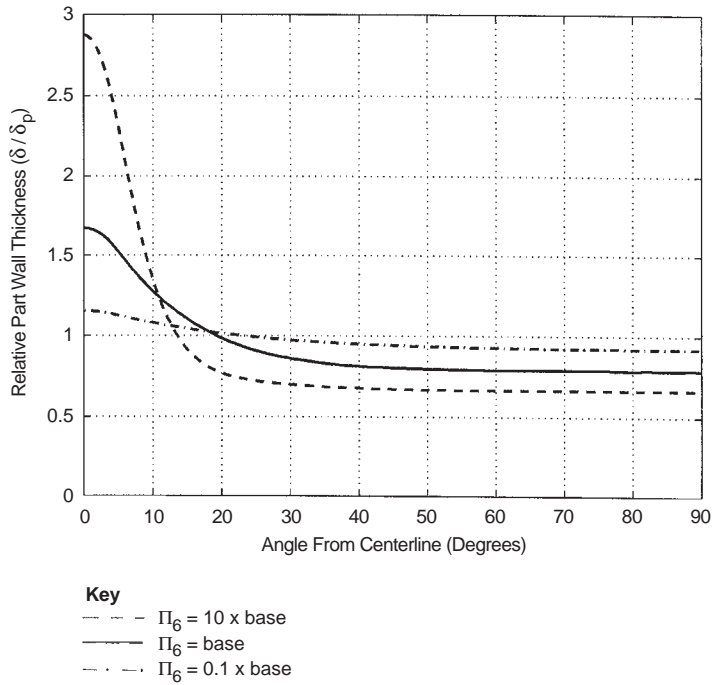


**Figure 16.**  
Effect of variations in  $\Pi_6 = k_p/(\delta_p h_o)$  on plastic layer profiles. Base case with  $hw/h_oR = 0.400$  and  $w/R = 0.077$  ( $4^\circ$ )

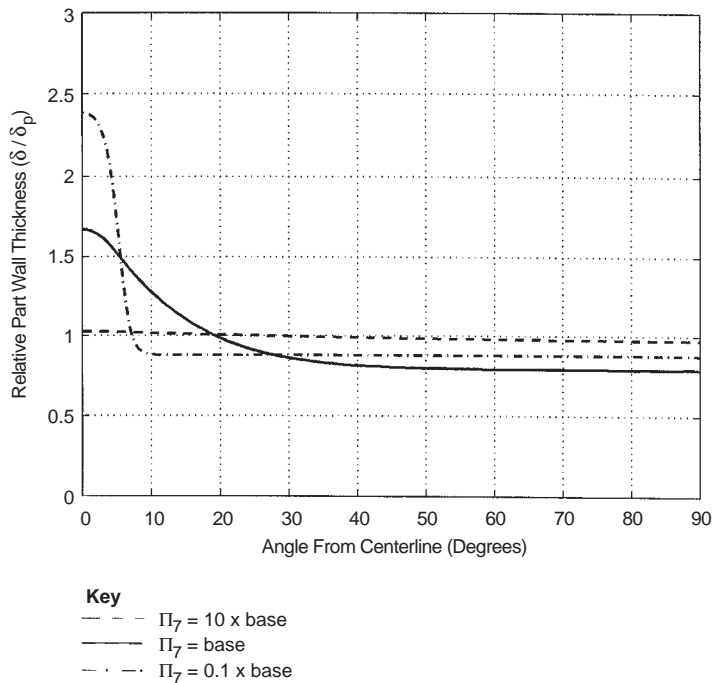


**Figure 17.**  
Effect of variations in  $\Pi_7 = \delta_m/R$  on plastic layer profiles. Base case with  $hw/h_oR = 0.400$  and  $w/R = 0.077$  ( $4^\circ$ )

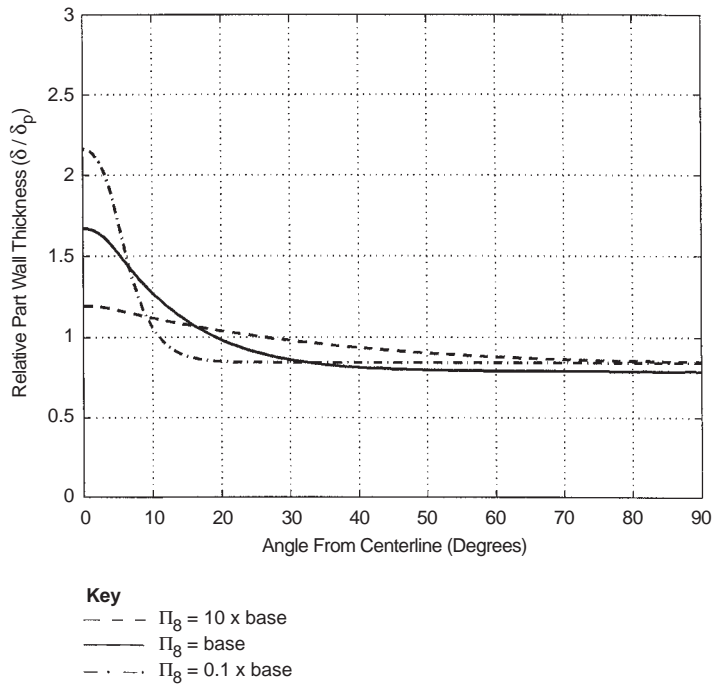


**Figure 18.**  
Effect of variations in  $\Pi_8 = k_m(\delta_m/h_o)$  on plastic layer profiles. Base case with  $hw/h_oR = 0.400$  and  $w/R = 0.077$  ( $4^\circ$ )

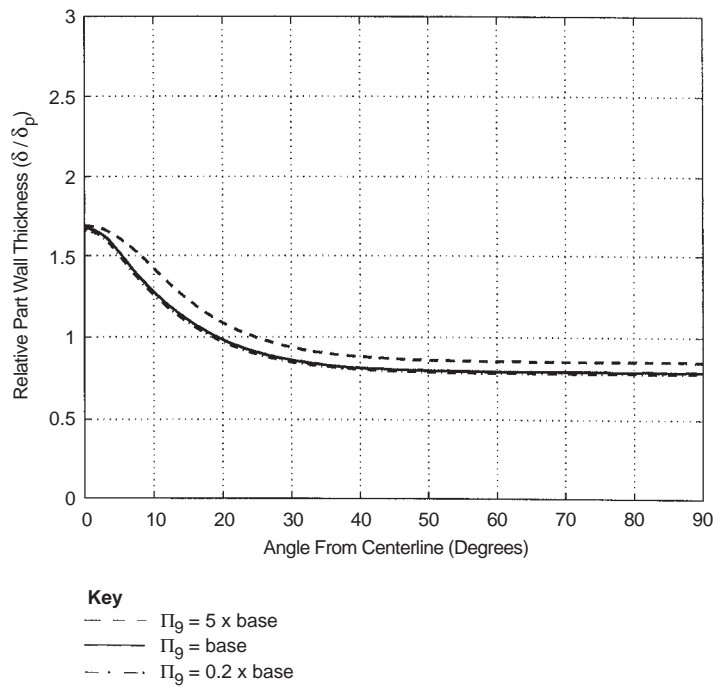


**Figure 19.**  
Effect of variations in  $\Pi_9 = \delta_p/R$  on plastic layer profiles. Base case with  $hw/h_oR = 0.400$  and  $w/R = 0.077$  ( $4^\circ$ )

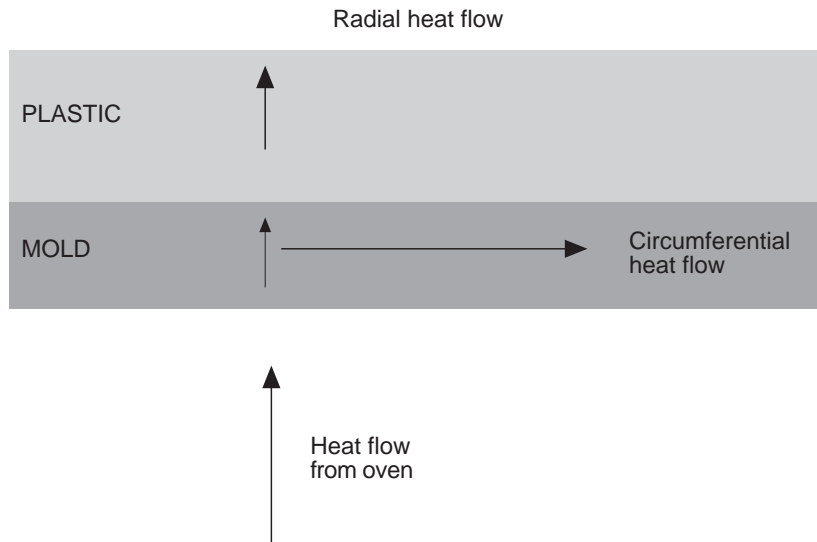


**Figure 20.**  
Heat flow paths

reduced by half, to 1.05mm. The resulting ribs are shown in Figure 21. For the “narrow” rib,  $w/R$  was held at 0.077 ( $4^\circ$ ), while the heat transfer coefficient in the enhanced heat transfer region was decreased so that  $hw/h_oR = 0.321$  (to reduce the height of the rib). This “narrow” rib is much better defined than in the base case, although its width is still controlled by mold/plastic conductivities rather than the enhanced heat transfer region width of  $4^\circ$ . The “wide” rib employed an enhanced heat transfer region with  $w/R = 0.397(23^\circ)$  and  $hw/h_oR = 1.646$  (to increase the height of the rib). This rib has a width which closely reproduces the enhanced heat transfer region.

### Conclusions and future work

We have presented a new axisymmetric finite element method for the rotational molding process. The method employs the single powder temperature model of Gogos and Olson (1998). The nonlinear finite element method developed is applicable through the end of powder deposition, and employs arbitrary Lagrangian Eulerian techniques to track the gradual and nonuniform deposition of the plastic layer on the inner surface of the mold. Results compare well with computational results obtained with one-dimensional models, and show good agreement with experimental data from the literature.

Using this finite element method, we have also studied the effect of locally enhanced heat transfer on part wall thicknesses. By examining the various dimensionless groups operating in rotational molding, we can identify important heat transfer parameters for the control of plastic deposition. We found that the relative importance of radial and circumferential heat transfer is crucial in obtaining desired plastic layer profiles. This leads us to conclude that

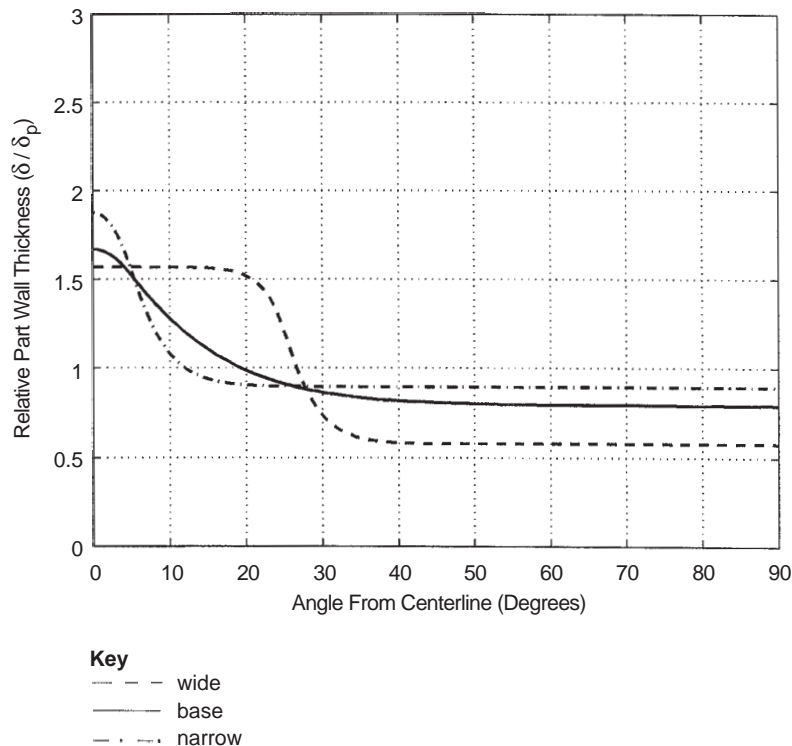


**Figure 21.** Base, wide and narrow ribs. Base case with 2.1mm mild steel mold,  $hw/h_oR = 0.400$  and  $w/R = 0.077$  ( $4^\circ$ ). Wide case with 1.05mm stainless steel mold,  $hw/h_oR = 0.321$  and  $w/R = 0.077$  ( $4^\circ$ ). Narrow case with 1.05mm stainless steel mold  $hw/h_oR = 1.646$  and  $w/R = 0.397$  ( $23^\circ$ )

good control of plastic layer profiles through the use of enhanced heat transfer can only be obtained when circumferential heat transfer is limited by the use of thin, relatively low conductivity mold materials.

In the future we will examine cooling and solidification of rotationally molded parts in a multidimensional setting. In this context we hope to examine the effects of the kinetics of solidification, and ultimately compute stresses and related part-mold separation in general rotationally molded parts.

**Note**

1. For computational purposes, the volume of the elements is set to a small positive value ( $4 \times 10^{-12}$ ).

**References**

Bathe, K.J. (1996), *Finite Element Procedures*, Prentice-Hall Inc., Englewood Cliffs, NJ.  
 Crawford, R.J. (Ed.) (1996), *Rotational Molding of Plastics*, 2nd ed., Research Studies Press Ltd and John Wiley & Sons Inc.  
 Ghosh, S. and Kikuchi, N. (1991), "An arbitrary Lagrangian-Eulerian finite element method for large deformation analysis of elastic-viscoplastic solids", *Computer Methods in Applied Mechanics and Engineering*, Vol. 86, pp. 127-88.

- Ghosh, S. and Moorthy, S. (1993), "An arbitrary Lagrangian-Eulerian finite element model for heat transfer analysis of solidification processes", *Numerical Heat Transfer, Part B*, Vol. 23, pp. 327-50.
- Gogos, G., Liu, X. and Olson, L.G. (1999), "Cycle time predictions for the rotational molding process with and without mold/part separation", *Polymer Engineering and Science*, in press.
- Gogos, G., Olson, L., Liu, X. and Pasham, V. (1997a), "Computational model for rotational molding of thermoplastics", *SPE ANTEC Technical Papers* 21.
- Gogos, G.L., Olson, L., Liu, X. and Pasham, V. (1997b), "A model for rotational molding of thermoplastics", *Transactions of the North American Manufacturing Research Institution of the Society of Manufacturing Engineers*, Vol. 25, pp. 13-17.
- Gogos, G., Olson, L.G., Liu, X. and Pasham, V.R. (1998), "New models for rotational molding of plastics", *Polymer Engineering and Science*, Vol. 38 No. 9, p. 1387-98.
- Hu, Y.-K. and Liu, W.K. (1993), "An ALE hydrodynamic finite element method with application to strip rolling", *International Journal for Numerical Methods in Engineering*, Vol. 36, pp. 855-80.
- Liu, W.K., Hu, Y.-K. and Belytschko, T. (1992), "ALE finite elements with hydrodynamic lubrication for metal forming", *Nuclear Engineering and Design*, Vol. 138, pp. 1-10.
- Nitikitpaiboon, C. and Bathe, K.J. (1993), "An arbitrary Lagrangian-Eulerian velocity potential; formulation for fluid-structure interaction", *Computers and Structures*, Vol. 47, pp. 871-91.
- Nomura, T. and Hughes, T.J.R. (1992), "An arbitrary Lagrangian-Eulerian finite element method for interaction of fluid and a rigid body", *Computer Methods in Applied Mechanics and Engineering*, Vol. 95, pp. 115-38.
- Nugent, P.J. (1990), "Theoretical and experimental studies of heat transfer during rotational molding process", PhD thesis, Queen's University, Belfast.
- Nugent, P.J., Crawford, R.J. and Xu, L. (1992), "Computer prediction of cycle times during rotational molding of plastics", *Advances in Polymer Technology*, Vol. 11 No. 3, pp. 181-91.
- Olson, L., Gogos, G., Pasham, V. and Liu, X. (1997), "Numerical modeling for rotational molding of thermoplastics", *Proceedings of the ASME Heat Transfer Division*, Vol. 1, pp. 113-19.
- Rao, M.A. and Thorne, J.L. (1972), "Principles of rotational molding", *Polymer Engineering and Science*, Vol. 12 No. 4, July, pp. 237-64.
- Schmidt, F.W., Henderson, R.E. and Wolgemuth, C.H. (1993), *Introduction to Thermal Sciences*, 2nd ed., John Wiley & Sons Inc.
- Sun, D.-W. and Crawford, R.J. (1993), "Analysis of the effects of internal heating and cooling during the rotational molding of plastics", *Polymer Engineering and Science*, Vol. 33 No. 3, February, pp. 132-9.
- Tadmor, Z. and Gogos, C.G. (1979), *Principles of Polymer Processing*, John Wiley & Sons Inc., New York, NY.
- Throne, J.L. (1976), "Rotational molding heat transfer – an update", *Polymer Engineering and Science*, Vol. 16 No. 4, April, pp. 257-64.